Available online at www.sciencedirect.com
ScienceDirect
Comput. Methods Appl. Mech. Engrg. 197 (2008) 3174–3181
Computer methods in applied mechanics and engineering
www.elsevier.com/locate/cma

Simulating nanoindentation and predicting dislocation nucleation using interatomic potential finite element method

Yuan Zhong, Ting Zhu *

Woodruff School of Mechanical Engineering, Georgia Institute of Technology, Atlanta, GA 30032, USA

Received 7 September 2007; received in revised form 23 September 2007; accepted 8 October 2007
Available online 26 December 2007

Abstract

Dislocation nucleation is central to our understanding of the onset of plasticity during nanoindentation. The shear stress in small volumes beneath the nanoindenter can achieve the theoretical limit of a perfect crystal. The ensuing nonlinear elastic instability can trigger homogenous dislocation nucleation inside the crystal. Here we employ the interatomic potential finite element method to simulate nanoindentation and predict dislocation nucleation. Simulations are performed for indentation on the (1 1 1), (1 1 0) and (1 0 0) surfaces of Al, Cu, Ni single crystals. We quantify the critical conditions of dislocation nucleation, including the indentation load of nucleation, location of nucleation site, nucleation stress and activated slip system. We find these conditions sensitively depend on indentation orientation, but are consistent for different crystals. The results highlight the critical role of hyperelasticity (the nonlinear elasticity caused by elastic softening at large strain) and crystallography in dislocation nucleation in small material volumes. Our study also reveals the deficiency of commonly used nucleation criterion such as the critical resolved shear stress.

Keywords: Interatomic potential finite element method; Nanoindentation; Dislocation nucleation

1. Introduction

In nanoindentation experiments, the shear stress at the onset of plasticity can approach the theoretical shear strength of a perfect crystal [1–6]. Such ultra-high stress occurs in small (nanometer-sized) volumes beneath the nanoindenter, which can be free of any pre-existing defects. A defect-free crystal deforms in a nonlinear manner, when the shear stress approaches the theoretical limit. The nonlinear elastic, or the so-called hyperelastic, response arises from the elastic softening of crystal lattice at large strain. This paper is concerned with the critical role of hyperelasticity, as well as crystallography, in the onset of plasticity during nanoindentation, a process arguably associated with homogenous dislocation nucleation that result from the nonlinear elastic instability of crystal at large shear.

Here we employ the interatomic potential finite element method (IPFEM) [7–9] to simulate nanoindentation and predict homogenous dislocation nucleation. The IPFEM simulation takes as an input the interatomic potential-based constitutive relation derived within the framework of hyperelasticity of single crystals [10]. It can accurately capture the essential physical effects of crystal at large deformation: *nonlinear elasticity* and *shear asymmetry* (i.e., the asymmetry of shear stress with respect to the sense of shearing in the Shockley partial direction of $\{1\,1\,1\}\langle 1\,1\,\bar{2}\rangle$), thereby enabling an accurate prediction of dislocation nucleation. Compared to the commonly used molecular dynamics (MD), the IPFEM significantly improves the computational efficiency, so that the effects of system size and loading rate can be minimized, and consequently simulations of nanoindentation can be performed on the length and time scales close to laboratory experiments.

In this study, simulations are performed for nanoindentation on several face-centered cubic (fcc) crystals at low

* Corresponding author. Tel.: +1 404 894 6597.
E-mail address: ting.zhu@me.gatech.edu (T. Zhu).

0045-7825/$ - see front matter © 2007 Elsevier B.V. All rights reserved.
doi:10.1016/j.cma.2007.10.009

temperature (nearly zero-K) when the effect of thermal activation is negligible. For each crystal, we simulate indentation on the (1 1 1), (1 1 0) and (1 0 0) surfaces, and quantify the critical conditions of homogenous dislocation nucleation in the bulk perfect crystal. The results highlight the central role of hyperelasticity (nonlinear elasticity) and crystallography in dislocation nucleation in small material volumes, a process requiring ultra-high stress that is achievable during nanoindentation. Our study also reveals the deficiency of commonly used nucleation criterion such as the critical resolved shear stress. With the rapid development in the experimental techniques of nanoindentation [6], we envision a direct comparison will soon become possible between the experiments (where a further improvement for quantitative control is needed) and atomistics-based quantification of critical conditions of dislocation nucleation as predicted in this paper.

2. Method

2.1. Interatomic potential finite element method

The key to the interatomic potential finite element method (IPFEM) is the interatomic potential-based constitutive relation derived within the framework of hyperelasticity with the Cauchy–Born rule [10]. The basic premise of this approach is that every point in a continuum corresponds to a large region of uniformly deformed lattice at the atomic scale. It follows that the energy of a continuum point can be calculated by summing the energy of the underlying lattice deformed according to the continuum deformation gradient, F_{ij}. Specifically, for a continuum point, all underlying atoms are identical, one may consider the energy of one atom at the origin to be representative, and calculate the energy associated with this atom; the energy density is the energy per atom divided by the atomic volume. Within the framework of the embedded-atom method (EAM) [11], and consider the crystal at nearly zero-K temperature, the energy density W is given by

$$W = \frac{1}{\Omega_0}\left[\sum_K V(r^K) + U(\bar{\rho})\right], \tag{1}$$

where $V(r^K)$ is the pair potential, $\bar{\rho} = \sum_K \rho(r^K)$ is the ambient electron density for the atom at the origin, and $U(\bar{\rho})$ is the energy required to embed this atom into the electron density. In Eq. (1), Ω_0 is the atomic volume in a stress free fcc lattice, namely, $\Omega_0 = a_0^3/4$, where a_0 is lattice constant; r^K denotes the distance between the atom at the origin and a neighboring atom when the lattice is deformed, here, the index K runs over all atoms within a cut-off radius R_c prescribed by the interatomic potential.

The Cauchy (true) stress can be obtained using the standard relation between energy density and stress,

$$\sigma_{ij} = \frac{1}{\det(F_{ij})} F_{im} F_{jn} \frac{\partial W}{\partial E_{mn}}. \tag{2}$$

In Eq. (2), the Green strain E_{ij} is defined as $E_{ij} = \frac{1}{2}(F_{ki}F_{kj} - \delta_{ij})$, where δ_{ij} denotes the Kronecker delta; the energy density W, as defined in Eq. (1) depends on E_{ij} through $r^K = \sqrt{(\delta_{ij} + 2E_{ij})x_{0i}^K x_{0j}^K}$, where x_{0j}^K is the coordinate of a neighboring atom in the stress-free fcc lattice. Substitution of Eq. (1) into Eq. (2) leads to

$$\sigma_{ij} = \frac{1}{\det(F_{ij})\Omega_0} \times \sum_K \left[\frac{1}{2}\frac{\partial V(r^K)}{\partial r} + \frac{\partial U(\bar{\rho})}{\partial \bar{\rho}}\frac{\partial \rho(r^K)}{\partial r}\right]\frac{x_i^K x_j^K}{r^K}. \tag{3}$$

Here x_j^K denotes the Cartesian coordinate of a neighboring atom in the deformed lattice, and it can be calculated by $x_j^K = F_{ij}x_{0j}^K$. Since the Cauchy stress in Eq. (3) involves lattice sum and nonlinear functions of $V(r^K)$, $U(\bar{\rho})$ and $\rho(r^K)$ [12,13], the effects of crystal anisotropy and nonlinear elasticity are incorporated automatically.

The tangent modulus, c_{ijkl}, can also be calculated from the interatomic potential, as detailed in [9],

$$c_{ijkl} = \frac{1}{\det(F_{ij})\Omega_0}\left\{\sum_K \left[\frac{1}{2}\left(\frac{\partial V^2(r^K)}{\partial r^2} - \frac{1}{r^K}\frac{\partial V(r^K)}{\partial r}\right) + \frac{\partial U(\bar{\rho})}{\partial \bar{\rho}}\left(\frac{\partial^2 \rho(r^K)}{\partial r^2} - \frac{1}{r^K}\frac{\partial \rho(r^K)}{\partial r}\right)\right]\frac{x_i^K x_j^K x_k^K x_l^K}{(r^K)^2} + \frac{\partial^2 U(\bar{\rho})}{\partial \bar{\rho}^2}\left(\sum_K \frac{\partial \rho(r^K)}{\partial r}\frac{x_i^K x_j^K}{r^K}\right)\left(\sum_K \frac{\partial \rho(r^K)}{\partial r}\frac{x_k^K x_l^K}{r^K}\right)\right\}. \tag{4}$$

Here, the current and reference configurations are assumed to coincide. Because of the elastic softening of the hyperelastic crystal, the prediction of dislocation nucleation (see Section 2.3) requires an update of the tangent modulus c_{ijkl} when deformation gradient F_{ij} changes.

The above interatomic potential-based constitutive model can accurately describe the hyperelastic response of a bulk crystal, whereas it is inadequate to model the elastic behavior of atomic layers near the crystal surface [14], where atoms are mis-coordinated compared to the perfect crystal. However, since we will consider the indenter with a tip radius of 50 nm (an approximate size in experiments), the nucleation sites are located at about 10 nm below the contact surface, so that the effect of mis-coordinated surface atoms are negligible. As such, this constitutive model is sufficient to study nanoindentation-induced dislocation nucleation inside the bulk crystal, as verified by molecular dynamics simulations [9].

The interatomic interactions are modeled using the EAM potentials [11], which can better describe the many-body effects of metallic bonding compared to the two-body pair potential such as Lennard–Jones potential. The EAM potentials used in this study are developed by Mishin et al. [12,13], which have been validated by comparing with experimental results (if available) and/or ab initio calculations. Table 1 compares the elastic constants of the

Table 1
Elastic constants of stress-free single crystals of Cu, Ni and Al

		c_{11} (GPa)	c_{12} (GPa)	c_{44} (GPa)	$\beta \equiv \frac{2c_{44}}{c_{11}-c_{12}}$
Cu	Experiment	168.4	121.4	75.4	3.2
	Potential	169.9	122.6	76.2	
Ni	Experiment	247	147	125	2.5
	Potential	247	148	125	
Al	Experiment	114	61.9	31.6	1.2
	Potential	114	61.6	31.6	

Predictions by the EAM potentials are compared with experimental data. $\beta \equiv 2c_{44}/(c_{11} - c_{12})$ measures the degree of crystal anisotropy.

stress-free crystals (Cu/Ni/Al) between experiments and predictions by the potentials. It also lists the crystal-anisotropy parameter $\beta \equiv 2c_{44}/(c_{11} - c_{12})$; for isotropic materials, $\beta = 1$.

We have implemented this interatomic potential-based hyperelastic model for the fcc crystals of Cu, Al and Ni in the finite element program ABAQUS/Explicit (2006) by writing user material subroutines. In the dynamic, explicit computational procedures of this program, as detailed in ABAQUS Theory Manual [15], the nonlinear response is obtained incrementally, given the internal forces created by the stresses in the elements, as well as the applied external forces at the start of an increment, time t. Finite element procedures solve for the acceleration at the start of the increment by solving the discretized local equations of motion. The velocities at time $t + \Delta t/2$ and the displacements at time $t + \Delta t$ are updated by a central difference time-integration procedure. The deformation gradient F_{ij} for each integration point at time $t + \Delta t$ is then calculated based on the updated displacement field. Given the calculated deformation gradient, a constitutive equation subroutine, called VUMAT in ABAQUS/Explicit, is required in order to determine the stress in the element at time $t + \Delta t$. In the implementation of stress calculation according to Eq. (3), each material point (integration point) is represented by an fcc lattice, which deforms according to the local continuum deformation gradient F_{ij}. That is, at the beginning of the calculation ($t = 0$), a set of neighboring atoms is created to represent the atomic environment of the central atom at the origin, e.g., an atom in the first neighboring shell should be located at ($a_0/2$, $a_0/2$, 0), an atom in the second neighboring shell is at (a_0, 0, 0), etc. Here, the lattice spacing a_0 is chosen such that the Cauchy stress is zero at $t = 0$, and the number of included neighboring atoms is determined by the cut-off radius prescribed by interatomic potentials [12,13]. For each time increment, the neighboring atoms update their positions according to the local deformation gradient F_{ij}, which is generated according to the imposed boundary conditions. Then the Cauchy stress σ_{ij} and tangent modulus c_{ijkl} are calculated by substituting the deformed positions of neighboring atoms into Eqs. (3) and (4), respectively. Thus, material properties depend exclusively on the atomistic description of the system.

2.2. Nonlinear elasticity and shear asymmetry at large strain

In this section, we highlight the important features of the interatomic potential-based constitutive model: *nonlinear elasticity* and *shear asymmetry* at large strain. Consider an fcc crystal undergoing uniform simple shear in the Shockley partial direction of $\{1\,1\,1\}\langle 1\,1\,\bar{2}\rangle$. Fig. 1 shows the shear stress–strain curves predicted by the EAM potentials. Evidently, the crystal at large shear exhibits nonlinearity and asymmetry of shear stress with respect to the sense of shearing in the $\langle 1\,1\,\bar{2}\rangle$ direction. The former can be attributed to the elastic softening at large strain, whereas the latter arises because of the asymmetric packing of atoms in the $\langle 1\,1\,\bar{2}\rangle$ direction [9]. The two effects critically control when, where and how a dislocation homogeneously nucleates beneath the indenter, as detailed in Section 3.

2.3. Dislocation nucleation criterion

Homogenous dislocation nucleation in the bulk perfect crystal can be triggered by the nonlinear elastic instability of crystal at large deformation. The onset of instability is associated with the Hadamard condition of loss of positive definiteness of the matrix Q_{jk} defined by

$$Q_{jk} = n_i(c_{ijkl} + \sigma_{jk}\delta_{il})n_l \tag{5}$$

for any unit vector n_i [16,17]. Here, the current and reference configurations are assumed to coincide; σ_{jk} is the Cauchy (true) stress and c_{ijkl} is the tangent (instantaneous elastic) modulus, both of which are calculated from the interatomic potential, see Eqs. (3) and (4). For small deformations, Q_{jk} is positive definite. When

$$\det(Q_{jk}) = 0, \tag{6}$$

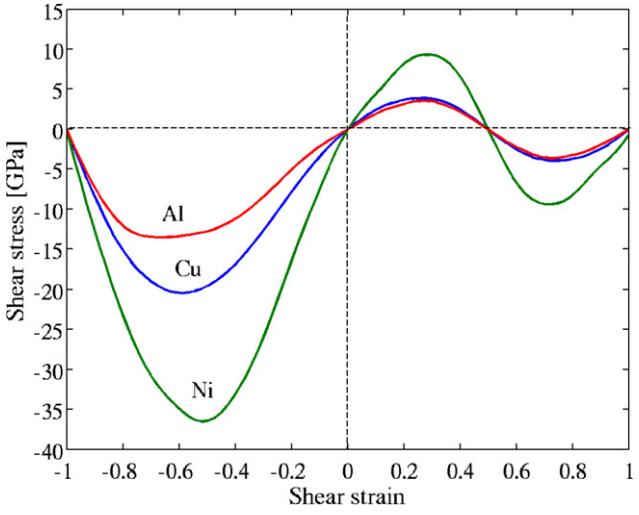

Fig. 1. Stress–strain curves for simple shear of single crystals of Al, Cu, Ni in the Shockley partial direction of $\{1\,1\,1\}\langle 1\,1\,\bar{2}\rangle$, showing the nonlinear elasticity and asymmetry of shear stress with respect to the sense of shearing at large deformation.

loss of stability occurs, leading to dislocation nucleation. Correspondingly, the unit vector n_i predicts the activated slip plane, and the eigenvector g_i associated with the matrix Q_{jk} predicts the slip direction at the onset of dislocation formation. By comparing with MD simulations, we have quantitatively verified the accuracy of this nucleation criterion in terms of the predictions of the critical indentation load, location of nucleation site and activated slip systems [9].

To appreciate the key difference between the nucleation criterion of Eq. (6) with the commonly used one such as the critical resolved shear stress (CRSS), we note that Q_{jk} in Eq. (6) contains both the tangent modulus c_{ijkl} and Cauchy (true) stress σ_{jk}. When a dislocation is about to nucleate (the corresponding shear strain is large), the magnitudes of c_{ijkl} and σ_{jk} become comparable due to elastic softening of the hyperelastic crystal; the nucleation criterion of Eq. (6) states that when the decreasing c_{ijkl} is balanced with the increasing σ_{jk}, the crystal becomes unstable, leading to homogenous dislocation nucleation. Since the instability does not occur precisely when the tangent modulus vanishes (equivalently, the RSS maximizes), the nucleation criterion based on the CRSS is not accurate. Moreover, the CRSS is not a material constant; it depends on other stress components than just the shear. Thus, even an approximate use of CRSS to predict nucleation would require a calibration for different stress (deformation) states, similar to the construction of a yield surface in stress space in the plasticity theory. In contrast, the nucleation criterion of Eq. (6) does not require calibration; nucleation occurs as a natural consequence of loss of positive definiteness of the matrix Q_{jk}.

2.4. Simulation setup

Using the IPFEM, we have performed 3D simulations of nanoindentation by a spherical indenter, and quantified the critical states of dislocation nucleation. Predictions will be given as to when and where the dislocation will nucleate within the crystal, and what slip mode the nucleated dislocation will take. More specifically, indentation is simulated for a spherical indenter pressed into the (1 1 1), (1 1 0) and (1 0 0) surfaces of single crystals of Al, Cu, Ni. The radius of the indenter is 50 nm, the approximate tip size of a nominally sharp Berkovich indenter used in typical nanoindentation experiments. The spherical indenter is modeled as a frictionless, analytic rigid surface. Since this research is focused on dislocation nucleation inside the bulk crystal, the effects of indenter elasticity and contact adhesion are ignored. However, those effects could play an important role if a dislocation nucleate directly from the contact surface [18,19]; a detailed study of surface nucleation is beyond the scope of this work. We have previously performed extensive numerical testing to assess the influences of geometry of simulation cell, imposed far-field boundary conditions, element type, and node density by comparing with the Hertzian solutions for the isotropic and anisotropic, linear elastic material, as detailed in [9]. We found for a system with the in-plane size of 300×300 and depth of 600 nm, the effect of boundary constraint is sufficiently minimized. To reduce the computational cost, we simulate one half of the whole system considering the cubic symmetry of crystal, as shown in Fig. 2. The boundary conditions are imposed as follows: the displacement along the bottom of the mesh is constrained to be zero, while the displacements of lateral surfaces are unconstrained. The graded mesh comprises 8-node linear brick elements, with typical size of elements near the indenter about 10 Å. The total number of elements is 519,332. Indenter is moved down in displacement control at a sufficiently low rate to mimic the quasi-static loading condition, as calibrated by the analytic solutions for indentation on a linear anisotropic elastic material [9].

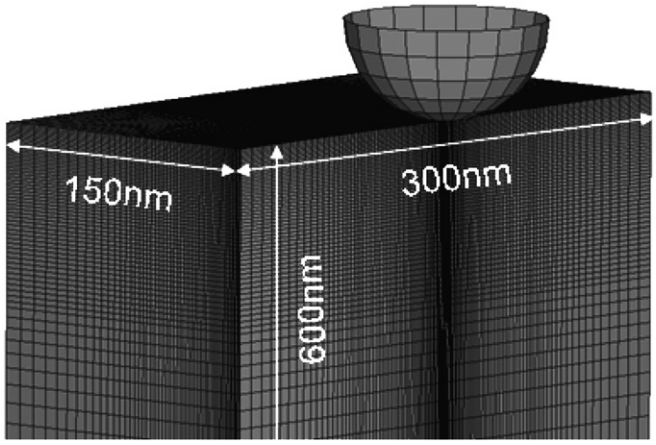

Fig. 2. Finite element mesh for indentation simulation. The spherical indenter is modeled as a frictionless, analytic rigid surface. The simulation cell is one half of the whole system considering the cubic symmetry of the fcc crystal.

3. Results and discussions

3.1. Indentation load–displacement response

Fig. 3a–c show the load–displacement (P–h) curves for nanoindentation on single crystals of Al, Cu and Ni, respectively. For each crystal, the P–h curves are calculated for three indentation orientations (1 1 1)/(0 1 1)/(0 0 1). The different P–h responses arise because of the elastic anisotropy of single crystals. For Al, the three P–h curves are very close, consistent with the fact that Al is a nearly isotropic material ($\beta = 1.2$, see Table 1). As the elastic anisotropy increases, i.e., from $\beta = 2.5$ for Ni to $\beta = 3.2$ for Cu, the variation in the P–h responses also increases for different indentation orientations. These results are consistent with the variation of indentation moduli given in Table 2, where the crystal is simplified as a linear, anisotropic and elastic material; such simplification renders the indentation moduli analytically solvable, thus providing a quantitative reference to the numerical calculation for the hyperelastic

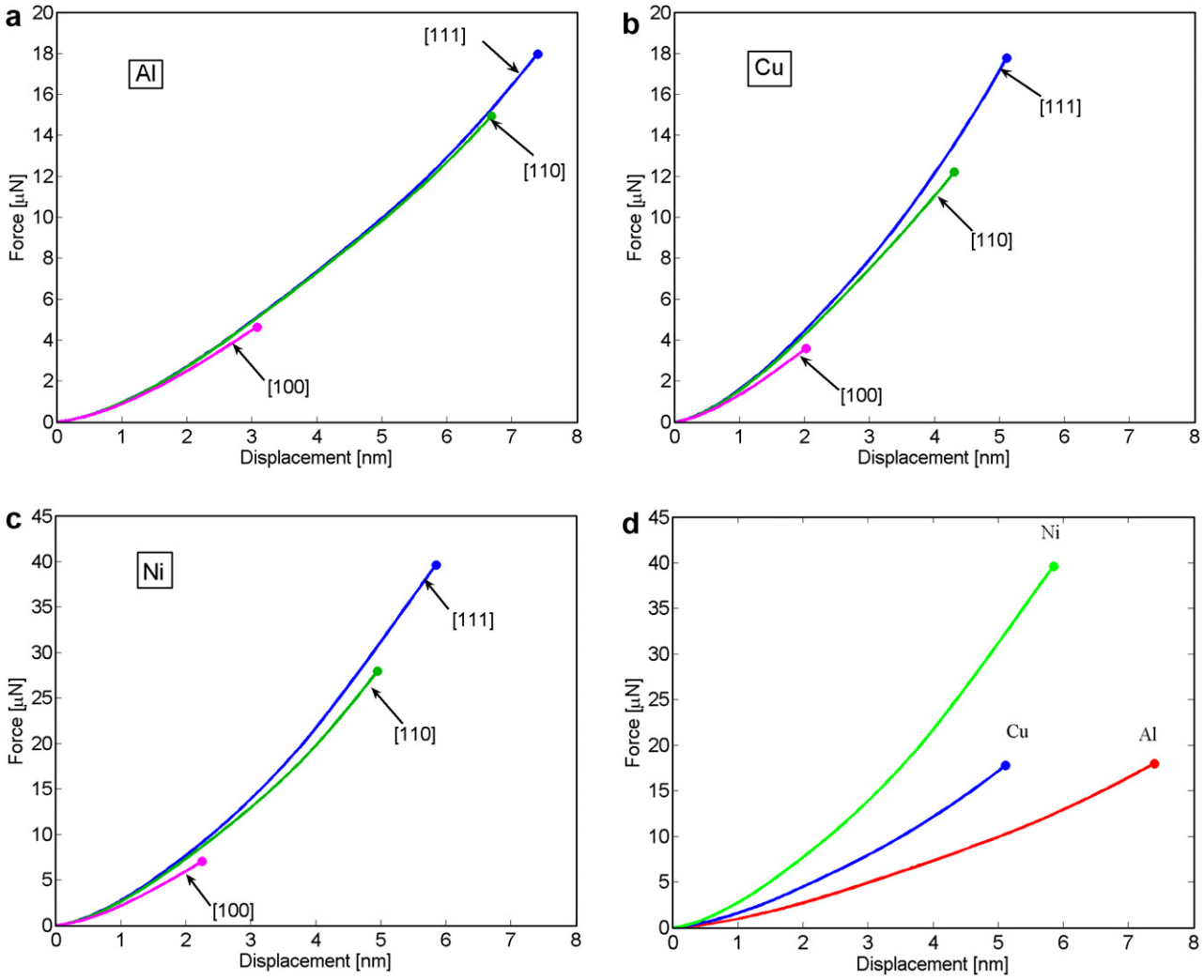

Fig. 3. Nanoindentation load–displacement curves for indentation on the (1 1 1), (1 1 0), (1 0 0) surfaces of single crystals of (a) Al, (b) Cu and (c) Ni. The (1 1 1) indentations are compared in (d) for the three crystals.

crystals. We note that the crystal beneath the nanoindenter should have undergone nonlinear elastic deformation before homogenous dislocation nucleation. But the effect of nonlinearity is not significant on the P–h response. This is because the P–h curve is not a particularly sensitive indicator on the nonlinear elastic deformation during nanoindentation, as it represents an average of the linear elastic response at the far field and the nonlinear elastic response close to indenter. However, the hyperelastic constitutive model, which is the basis of IPFEM simulations, is essential to predict dislocation nucleation caused by the nonlinear elastic instability of crystals at large shear, as shown in Section 3.3.

Table 2
Indentation moduli, E^*, for single crystals of Al, Cu and Ni

	$E^*_{(111)}$ (GPa)	$E^*_{(100)}$ (GPa)
Al	88.9	87.1
Cu	153	135
Ni	254	228

They are calculated by numerical integration using the semi-analytic indentation solution, with the elastic constants predicted by the interatomic potentials, as listed in Table 1. Specifically, when a cubic crystal deforms in the regime of linear anisotropic elasticity, the P–h response can be derived as $P = \frac{4}{3}E^* R^{1/2} h^{3/2}$ for a spherical indenter (radius R) on a half space; for the (1 1 1) and (1 0 0) indentations, it can be proven that the contact area is circular because of crystal symmetry, and the semi-analytic solution is given by [20,21].

In Fig. 3a–c, each P–h curve is terminated at an indentation depth (indicated by circle), when the onset of dislocation nucleation is first identified by the nucleation criterion of Eq. (6). For each crystal, the critical load of nucleation (P_c and h_c) changes considerably for different indentation orientations, e.g., $h_c^{\{111\}} : h_c^{\{110\}} : h_c^{\{100\}} \approx 5.04\text{ nm} : 3.85\text{ nm} : 1.93\text{ nm} \approx 2.6 : 2 : 1$ for Cu. This change arises because of the effect of crystallography, as first shown in Wang et al. [22]. Specifically, consider a simple situation of dislocation nucleation in the bulk single crystal under a uniaxial compressive stress σ. In this case

a dislocation tends to nucleate on one of the $\{1\,1\,1\}\langle 1\,1\,\bar{2}\rangle$ slip systems, where the resolved shear stress $\tau = m\sigma$ (m denotes the Schmid factor) first exceeds the shear resistance of nucleation in a perfect lattice. By considering the hard sphere packing of an fcc lattice and noting the effect of shear asymmetry as shown in Fig. 1, one can readily calculate m and identify the slip system of nucleation; for different compression orientations, the ratio of the inverse Schmid factor is $1/m^{\{1\,1\,1\}}$: $1/m^{\{1\,1\,0\}}$: $1/m^{\{1\,0\,0\}} = 3{:}2{:}1$. One may assume the shear resistance of nucleation τ_c is the same for each case, and then obtains $\sigma_c^{\{1\,1\,1\}} : \sigma_c^{\{1\,1\,0\}} : \sigma_c^{\{1\,0\,0\}} = 3:2:1$; here, in a first approximation we ignore the influence of other stress components on τ_c. The ratio of σ_c for different compression orientations is qualitatively consistent with that of the nucleation load h_c for different indentation orientations, thereby showing that the variation of h_c is dominantly controlled by the effect of crystallography. While the above simple analysis clarifies the controlling factor on h_c, the IPFEM calculations enable quantification of P_c and h_c by solving the distribution of nonuniform and nonlinear elastic deformation beneath the indenter, as shown in Fig. 3.

In Fig. 3d, we compare the P–h curves for the (1 1 1) indentation of the three crystals. It is seen that Ni is much stiffer than Cu and Al, consistent with the result that Ni has a higher indentation modulus as shown in Table 2. In terms of the critical indentation displacements of nucleation, h_c, it is interesting to note that although Cu and Al show very similar response for uniform simple shear (see Fig. 1), their h_c differ considerably; such difference arises because of crystal anisotropy, as well as the nonuniform deformation beneath the indenter, as manifested in the different indentation moduli (see Table 2).

3.2. Nucleation site and activated slip system

Fig. 4 shows the predicted nucleation sites from IPFEM calculations, using Al as an example. As schematically shown in Fig. 4a, the nucleation site for the (1 0 0) indentation is at the central loading axis. In contrast, it is off the central axis for the (1 1 0) and (1 1 1) indentations; the number of equivalent sites, as well as their locations, is dictated by crystal symmetry, see [9] for example. In Fig. 4b, we show the contours of $\det(Q_{jk})$ at the respective critical moment of nucleation and for the respective activated slip system. In each case, the gray element (highlighted with red circles) indicates the nucleation site directly visible on the surface of the simulation cell. Because of the high symmetry of indentation orientations, there are multiple equivalent slip systems at each site; the slip system first activated in experiment or MD simulation would be randomly selected by thermal fluctuations. Our predictions by IPFEM, which accurately incorporate the effects of elastic softening and crystal anisotropy, have been qualitatively verified by MD simulations [22]; but they are at variance with predictions based on the linear elastic analysis [23] and/or using the stress-based nucleation criterion such as the maximum equivalent shear stress or CRSS [24].

3.3. Critical resolved shear stress

We calculate the critical resolved shear stress (CRSS), τ_c, at the onset of nucleation, and show the CRSS is not an accurate nucleation criterion. Fig. 5 shows the indentation displacement versus RSS curves. The RSS, τ, is calculated at the critical nucleation site and for the activated slip system, according to $\tau = \sigma_{ij} n_i g_j$, where the current slip-plane

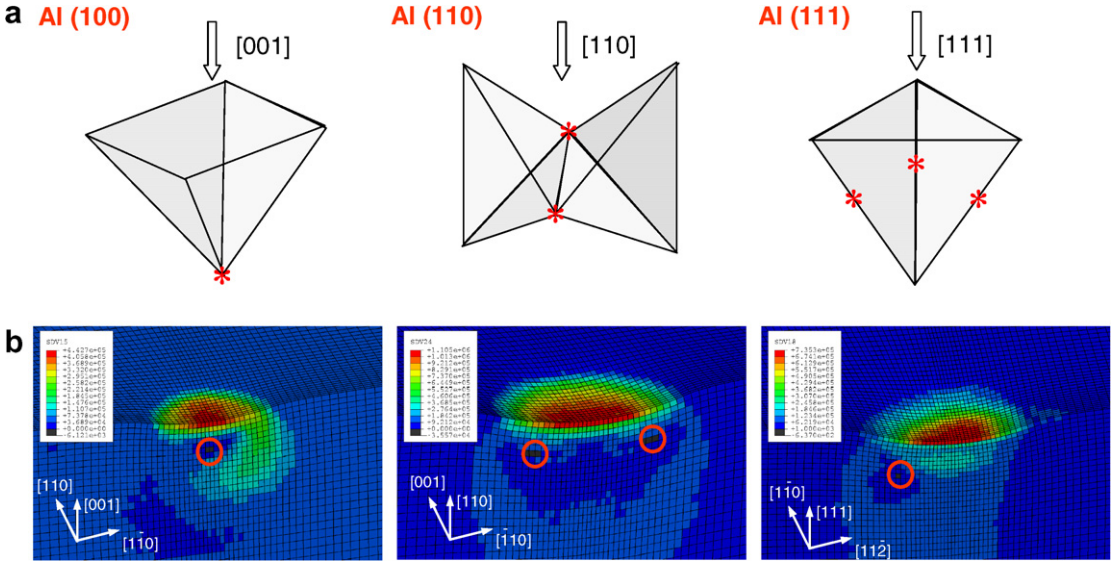

Fig. 4. IPFEM predictions of nucleation sites by nanoindentation on the (1 0 0), (1 1 0) and (1 1 1) surfaces of single crystal Al. (a) Schematics of location of nucleation sites; all the solid lines are in the $\langle 1\,1\,0\rangle$ directions and the shaded triangles represent the $\{1\,1\,1\}$ plane. (b) Contours of $\det(Q_{jk})$ at the respective critical moment of nucleation and for the respective activated slip plane. The gray element (highlighted with red circles) has a small negative value of $\det(Q_{jk})$, thus showing the nucleation sites. (For interpretation of the references to colour in this figure legend, the reader is referred to see the web version of this article.)

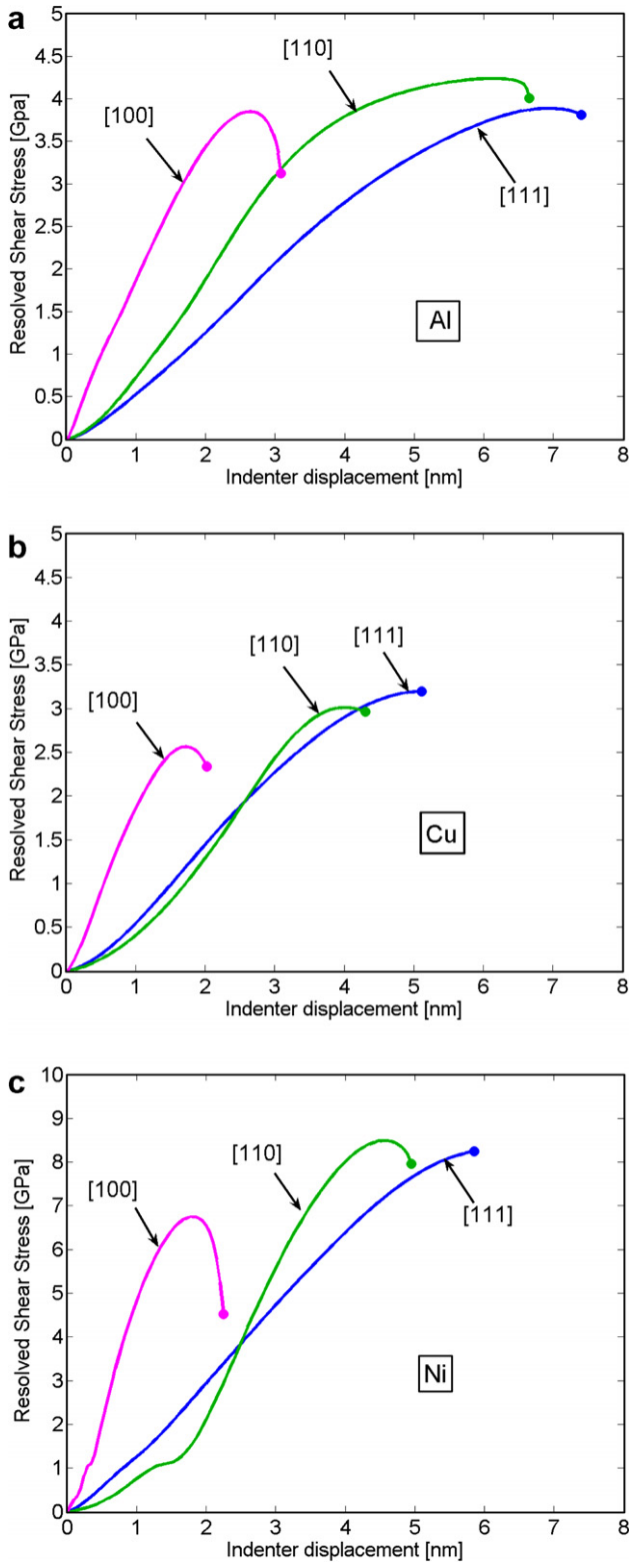

Fig. 5. Nanoindentation displacement versus resolved shear stress at the critical nucleation site and for the activated slip system for single crystals of Al, Cu and Ni.

normal, n_i, and slip direction, g_i, are related to those in the unformed crystal, n_{0j} and g_{0j}, by $n_i = n_{0j}F^{-1}_{ji}$ and $g_i = F_{ij}g_{0j}$, respectively. In Fig. 5, circle represents the CRSS, τ_c, when the nucleation criterion is first satisfied in IPFEM calculations. The respective τ_c is listed in Table 3 for the three crystals and three indentation orientations. Importantly, τ_c is not a constant for each crystal, and it depends on the indentation orientation. Fig. 5 also shows that τ_c is close to, but not right at the maximum of RSS. This is due to the elastic-softening effect associated with the hyperelastic crystals; namely, according to the physically based nucleation criterion of Eq. (5), the nucleation occurs when the tangent modulus c_{ijkl} is balanced with the Cauchy stress σ_{ij}, rather than when c_{ijkl} vanishes or equivalently the RSS maximizes. Hence, these results clearly demonstrate that the CRSS is NOT an accurate nucleation criterion; an approximate use of CRSS needs a calibration by combining experiments and IPFEM calculations.

Table 3
The critical resolved shear stress (CRSS) of dislocation nucleation at the respective nucleation site for nanoindentation of single crystals Al, Cu and Ni with three indentation orientations

	(111)	(110)	(100)
τ_c–Cu (GPa)	3.2	3.0	2.3
τ_c–Al (GPa)	3.8	4.0	3.1
τ_c–Ni (GPa)	8.2	8.0	4.5

Finally, we note that Fig. 5c reveals a numerical artifact of the RSS response for Ni under the (110) indentation, i.e., there is an abrupt change of the slope at low loads. Considering the overall reliable performance of the EAM potentials, which have been extensively calibrated by comparing with experimental or ab inito data [12,13], we believe such a small artifact should not affect the overall reliability of the results reported in this study.

4. Summary and conclusions

We have simulated nanoindentation and predicted dislocation nucleation in fcc single crystals of Al, Cu and Ni. Simulations are performed using the interatomic potential finite element method, which is a computationally efficient approach that facilitates the study at length scales large compared to atomic dimensions, while remaining faithful to the nonlinear interatomic interactions. We consider homogenous dislocation nucleation triggered by the nonlinear elastic instability of crystal at large strain and nearly zero-K temperature. The results show that the critical resolved shear stress of nucleation is at the GPa-level, close to the theoretical limit of perfect crystals. However, the critical conditions of dislocation nucleation, including the indentation load of nucleation, location of nucleation site, nucleation stress and activated slip systems, sensitively depend on the indentation orientation. But these conditions are consistent for different fcc crystals. Our study highlights the critical role of hyperelasticity (nonlinear elasticity) and crystallography in homogenous dislocation nucleation, and reveals the deficiency of commonly used nucleation criterion such as the critical resolved shear stress.

We conclude by commenting that for a complete understanding of defect formation by nanoindentation, one needs to take into account the influences of finite temperature [25], structural heterogeneities (e.g., surface step [18]), pre-existing dislocations [26], as well as the effect of homogenously nucleated dislocations on subsequent nucleation [7,27]. Recent development in the activation analysis of thermally activated dislocation nucleation at the interface [28], surface [29], and pre-existing defect [30,31], provides a viable approach to address these issues. With the results from this study as input (e.g., critical loads, nucleation sites and activated slip systems), we envision the activation analysis of nucleation during nanoindentation will enable a quantitative connection between experiments and modeling.

Acknowledgements

This work is supported by NSF Grant CMMI-0653769 and AFOSR/MURI Grant F49620-02-1-0382. We thank Ke Lu and Ju Li for stimulating discussions.

References

[1] T.F. Page, W.C. Oliver, C.J. McHargue, The deformation-behavior of ceramic crystals subjected to very low load (nano)indentations, J. Mater. Res. 7 (2) (1992) 450–473.
[2] W.W. Gerberich, J.C. Nelson, E.T. Lilleodden, P. Anderson, J.T. Wyrobek, Indentation induced dislocation nucleation: the initial yield point, Acta Mater. 44 (1996) 3585–3598.
[3] A. Gouldstone, H.J. Koh, K.Y. Zeng, A.E. Giannakopoulos, S. Suresh, Discrete and continuous deformation during nanoindentation of thin films, Acta Mater. 48 (2000) 2277–2295.
[4] W. Wang, K. Lu, Nanoindentation study on elastic and plastic anisotropies of Cu single crystals, Philos. Mag. 86 (2006) 5309–5320.
[5] A.M. Minor, S.A.S. Asif, Z.W. Shan, E.A. Stach, E. Cyrankowski, T.J. Wyrobek, O.L. Warren, A new view of the onset of plasticity during the nanoindentation of aluminium, Nat. Mater. 5 (2006) 697–702.
[6] A. Gouldstone, N. Chollacoop, M. Dao, J. Li, A.M. Minor, Y.L. Shen, Overview No. 142: indentation across size scales and disciplines: Recent developments in experimentation and modeling, Acta Mater. 55 (2007) 4015–4039.
[7] J. Li, K.J. Van Vliet, T. Zhu, S. Yip, S. Suresh, Atomistic mechanisms governing elastic limit and incipient plasticity in crystals, Nature 418 (6895) (2002) 307–310.
[8] K.J. Van Vliet, J. Li, T. Zhu, S. Yip, S. Suresh, Quantifying the early stages of plasticity through nanoscale experiments and simulations, Phys. Rev. B 67 (2003) 104105.
[9] T. Zhu, J. Li, K.J. Van Vliet, S. Ogata, S. Yip, S. Suresh, Predictive modeling of nanoindentation-induced homogeneous dislocation nucleation in copper, J. Mech. Phys. Solid 52 (2004) 691–724.
[10] J.L. Ericksen, The Cauchy and Born hypotheses for crystals, in: M.E. Gurtin (Ed.), Phase Transformations and Material Instabilities in Solids, Academic Press, New York, 1984, pp. 61–78.
[11] M.S. Daw, M.I. Baskes, Embedded-atom method – derivation and application to impurities, surfaces, and other defects in metals, Phys. Rev. B 29 (1984) 6443–6453.
[12] Y. Mishin, D. Farkas, M.J. Mehl, D.A. Papaconstantopoulos, Interatomic potentials for monoatomic metals from experimental data and ab initio calculations, Phys. Rev. B 59 (5) (1999) 3393–3407.
[13] Y. Mishin, M.J. Mehl, D.A. Papaconstantopoulos, A.F. Voter, J.D. Kress, Structural stability and lattice defects in copper: ab initio, tight-binding, and embedded-atom calculations, Phys. Rev. B 63 (22) (2001) 224106.
[14] H.S. Park, P.A. Klein, G.J. Wagner, A surface Cauchy–Born model for nanoscale materials, Int. J. Numer. Method Engrg. 68 (2006) 1072–1095.
[15] ABAQUS, Theory Manual. Hibbitt, Karlsson and Sorensen Inc., Pawtucket, R.I., 2006.
[16] R. Hill, Acceleration Waves in Solids, J. Mech. Phys. Solid 10 (1962) 1–16.
[17] J.R. Rice, The localization of plastic deformation, in: W.T. Koiter (Ed.), Proceedings of the 14th International Congress on Theoretical and Applied Mechanics, North-Holland Publishing Co., Amsterdam, 1976, pp. 207–220.
[18] J.A. Zimmerman, C.L. Kelchner, P.A. Klein, J.C. Hamilton, S.M. Foiles, Surface step effects on nanoindentation, Phys. Rev. Lett. 8716 (2001) 165507.
[19] H.H. Yu, P. Shrotriya, Y.F. Gao, K.S. Kim, Micro-plasticity of surface steps under adhesive contact: Part I – Surface yielding controlled by single-dislocation nucleation, J. Mech. Phys. Solid 55 (2007) 489–516.
[20] J.G. Swadener, G.M. Pharr, Indentation of elastically anisotropic half-spaces by cones and parabolae of revolution, Philos. Mag. A – Phys. Conden. Mat. Struct. Defect Mech. Proper. 81 (2001) 447–466.
[21] Y.F. Gao, G.M. Pharr, Multidimensional contact moduli of elastically anisotropic solids, Scripta Mater. 57 (2007) 13–16.
[22] W. Wang, Y. Zhong, T. Zhu, K. Lu, Quantifying the onset of plasticity during nanoindentation: experiment and modeling (in preparation).
[23] H. Bei, E.P. George, J.L. Hay, G.M. Pharr, Influence of indenter tip geometry on elastic deformation during nanoindentation, Phys. Rev. Lett. 95 (2005) 045501.
[24] T. Tsuru, Y. Shibutani, Anisotropic effects in elastic and incipient plastic deformation under (001), (1 1 0), and (1 1 1) nanoindentation of Al and Cu, Phys. Rev. B 75 (2007) 035415.
[25] C.A. Schuh, J.K. Mason, A.C. Lund, Quantitative insight into dislocation nucleation from high-temperature nanoindentation experiments, Nat. Mater. 4 (2005) 617–621.
[26] A.H.W. Ngan, P.C. Wo, Delayed plasticity in nanoindentation of annealed crystals, Philos. Mag. 86 (2006) 1287–1304.
[27] H.Y. Liang, C.H. Woo, H.C. Huang, A.H.W. Ngan, T.X. Yu, Crystalline plasticity on copper (001), (1 1 0), and (1 1 1) surfaces during nanoindentation, Cmes-Comput. Model. Engrg. Sci. 6 (2004) 105–114.
[28] T. Zhu, J. Li, A. Samanta, H.G. Kim, S. Suresh, Interfacial plasticity governs strain rate sensitivity and ductility in nanostructured metals, Proc. Natl. Acad. Sci. USA 104 (2007) 3031–3036.
[29] T. Zhu, J. Li, A. Samanta, A. Leach, K. Gall, Temperature and strain-rate dependence of surface dislocation nucleation, Phys. Rev. Lett., in press.
[30] T. Zhu, J. Li, S. Yip, Atomistic study of dislocation loop emission from a crack tip, Phys. Rev. Lett. 93 (2004) 025503.
[31] T. Zhu, J. Li, S. Yip, Atomistic configurations and energetics of crack extension in silicon, Phys. Rev. Lett. 93 (2004) 205504.